Available online at www.sciencedirect.com
ScienceDirect
Ceramics International 37 (2011) 1637–1644
CERAMICS INTERNATIONAL
www.elsevier.com/locate/ceramint

Synthesis, characterization and in vitro bioactivity of magnesium-doped sol–gel glass and glass-ceramics

J. Ma [a,b], C.Z. Chen [a,b,*], D.G. Wang [a,b], J.H. Hu [a,b]

[a] *Key Laboratory for Liquid–Solid Structural Evolution & Processing of Materials, Ministry of Education, Shandong University, Shandong, Ji'nan 250061, PR China*

[b] *School of Materials Science and Engineering, Shandong University, Shandong, Ji'nan 250061, PR China*

Received 28 April 2010; received in revised form 2 December 2010; accepted 21 January 2011
Available online 18 February 2011

Abstract

Bioactive glass and glass-ceramics in the system $CaO–MgO–SiO_2–P_2O_5$ have been prepared by the sol–gel and high temperature sintering techniques. The obtained samples were characterized by thermogravimetric and differential thermal analysis (TG/DTA), N_2-adsorption measurement, X-ray diffraction (XRD), Fourier transform infrared spectroscopy (FTIR) and scanning electron microscopy (SEM). In vitro bioactivity tests were also conducted in simulated body fluid (SBF). The studies of crystallization kinetics under non-isothermal conditions showed the activation energy for crystallization to be 381 kJ/mol and the crystallization mechanism gradually changed from three-dimension growth to two-dimension crystallization with the increase of heating rate. Sintering temperature had great influence on the samples texture and structure. In addition, the apatite-formation on glass and glass-ceramics was confirmed by in vitro tests, and crystallization decreased the samples bioactivity.

Keywords: D. Glass; D. Glass-ceramics; D. MgO; E. Biomedical applications

1. Introduction

Bioactive glasses and glass-ceramics have been extensively studied for more than thirty years since Hench et al. [1] reported bioglass in the system $SiO_2–Na_2O–CaO–P_2O_5$. At present, various types of bioactive glasses and glass-ceramics are under research and development, and a great effort is being put into the understanding of the mechanisms and factors governing their properties. A key feature of bioactive glasses and glass-ceramics is their ability to form an apatite-like layer on their surfaces in vivo and in vitro [2,3]. Due to ethic constrains related to the in vivo tests, in vitro tests (either in cellular or in acellular medium) have been extensively applied to evaluate the bioactive behavior of materials. For in vitro apatite formation, factors such as chemical composition, surface topography, texture (pore size and volume) and structure are believed to play an important role in the surface interaction of glasses and glass-ceramics with the surrounding medium [4–6].

Sol–gel technique provides an available way to prepare bioactive glasses. Compared with the traditional melting method, the sol–gel process is performed at lower temperature and it allows us to obtain glasses with higher purity and homogeneity. Furthermore, previous studies have demonstrated that sol–gel derived bioactive glasses possess higher index of bioactivity I_B ($I_B = 100/t_{0.5bb}$, where $t_{0.5bb}$ is the time for more than 50% of the implant interface to be bonded to bone) [7] and degradability.

Magnesium is an important trace element existing in human body. Enamel, dentin and bone contain 0.44, 1.23 and 0.72 wt.% of magnesium, respectively [8]. Moreover, magnesium has been shown to play an important role in bone development and maintenance [9,10]. Researchers substituted magnesium for calcium in biological hydroxyapatite and indicated that magnesium-substituted apatite materials had excellent biocompatibility and great osteoconductivity over time [11,12]. In addition, Vallet-Regí et al. [13] and Tahriri and co-workers [14,15] synthesized sol–gel derived glasses in the system $CaO–MgO–P_2O_5–SiO_2$. The apatite-formation ability

* Corresponding author at: Key Laboratory for Liquid–Solid Structural Evolution & Processing of Materials, Ministry of Education, Shandong University, Shandong, Ji'nan 250061, PR China. Tel.: +86 531 88395991; fax: +86 531 88395991.
E-mail address: czchen@sdu.edu.cn (C.Z. Chen).

0272-8842/$36.00
doi:10.1016/j.ceramint.2011.01.043

Table 1
Ion concentrations of SBF and human blood plasma (mM).

	Na^+	K^+	$Mg2^+$	$Ca2^+$	Cl^-	HCO_3^-	HPO_4^{2-}	SO_4^{2-}
SBF	142.0	5.0	1.5	2.5	148.8	4.2	1.0	0.5
Blood plasma	142.0	5.0	1.5	2.5	103.0	27.0	1.0	0.5

of glasses was confirmed by soaking them in a simulated body fluid (SBF), and in vitro experiments with human bone osteoblastic-like cells (HOB) suggested that bioactive glasses containing magnesium stimulated HOBs proliferation and differentiation. Therefore, in this work, we report the synthesis, characterization and in vitro bioactivity studies of sol–gel glass and glass-ceramics in the system CaO–MgO–P_2O_5–SiO_2 with 10 mol% MgO content.

2. Experimental

2.1. Synthesis

CaO–MgO–P_2O_5–SiO_2 (28% CaO, 10% MgO, 4% P_2O_5 and 58% SiO_2, based on mol%) quaternary system was prepared by the sol–gel method. The gel was synthesized by hydrolysis and polycondensation of stoichiometric amounts of tetraethyl orthosilicate ($Si(OC_2H_5)_4$, TEOS), triethyl phosphate ($OP(OC_2H_5)_3$, TEP), calcium nitrate tetrahydrate ($Ca(NO_3)_2{\cdot}4H_2O$) and magnesium nitrate hexahydrate ($Mg(NO_3)_2{\cdot}6H_2O$) in the presence of deionized water (mol of H_2O/(mole of TEOS + mole of TEP) = 10). Nitric acid (HNO_3, 2 N) was used as catalyst with a molecular ratio of HNO_3/(TEOS + TEP) = 0.05. The synthesis procedure was carried out as follows: the TEOS was mixed with deionized water and HNO_3, then TEP, $Ca(NO_3)_2{\cdot}4H_2O$ and $Mg(NO_3)_2{\cdot}6H_2O$ were successively added by keeping 1 h intervals between additions. After mixing all reagents, the solution was introduced into a sealed polyethylene container where it was allowed to gel at room temperature and aged at 60 °C for 3 days. Then the drying process was carried out at 130 °C for 6 h, followed by ball milling and sieving to obtain the xerogel with sizes ranging from 38 to 74 μm. Finally, the powders were respectively treated at 700, 900, 1000 and 1200 °C for 2 h, using a heating rate of 5 °C/min.

2.2. Characterization

Thermogravimetric and differential thermal analysis (TG/DTA) was carried on TA Instrument SDT Q600 simultaneous thermal analyzer. Non-isothermal experiment was performed by heating 15 mg xerogel powders in Pt crucible with Al_2O_3 as the reference material under an air atmosphere with a heating rate of 5–30 °C/min.

N_2-adsorption was performed using a Micromeritics ASAP2010 instrument. The specific surface area was obtained using the Barrett–Emmett–Teller (BET) method [16], while pore volume, average diameter and pore size distribution were determined from the isotherm desorption branch by the Barrett–Joyner–Halanda (BJH) method [17]. The powders were accurately measured by an FA2104 electronic balance with a 0.1 mg precision. Before measurements all samples were degassed at 120 °C for 2 h.

X-ray diffraction (XRD) patterns were obtained in a Bruker D8 Advance X-ray diffractometer using Cu Kα radiation produced at 40 kV and 40 mA. Data were collected from 10° to 70° 2θ with a scan rate of 4°/min and a step size of 0.02°.

Fourier transform infrared spectra (FTIR) were registered in a Bruker Optics VERTEX-70 spectrometer using KBr pellets. A total of 32 scan iterations were performed between 400 and 2000 cm^{-1} using a resolution of 4 cm^{-1}.

Scanning electron microscope (SEM) on a JEOL JSM-6380LA microscope system was conducted, and before tests samples were coated with a film of gold.

2.3. In vitro tests in SBF

In vitro tests were performed by soaking samples in SBF (pH 7.25) at 37 °C. The SBF proposed by Kokubo et al. [18] contains a similar ionic concentration as find in human blood plasma, as shown in Table 1. A mass to volume ratio of 0.1 g/100 ml was used and the SBF was continuously replaced every 2 days. After soaking, specimens were withdrawn from the solution, rinsed with deionized water and dried with acetone in air at room temperature. The formation of an apatite-like layer on the sample surface was determined by XRD, SEM and FTIR as described above.

3. Results and discussion

3.1. Thermal property analysis

Thermogravimetric and differential thermal analysis curves recorded at various heating rates are given in Fig. 1. The weight loss from TG curves shows three stages. The first weight loss between 60 and 170 °C is associated with the removal of physically adsorbed water, and it corresponds to an endothermic peak around 150 °C in DTA curves. The second commences from the end of the first weight loss (170 °C) until about 360 °C, which was attributed to the loss of organics. Then the third drop occurs from the end of the second weight loss (360 °C) until around 570 °C, with a sharp endothermic peak at 550 °C. This last process is attributed to the elimination of the residual nitrates introduced in the sol preparation. Afterwards, the weight remains constant up to 1100 °C. Furthermore, as shown in DTA curves, there is a small endothermic peak attributed to the glass transition temperature range; its minimum refers to the glass transition temperature (T_g). There is also an exothermic peak originating from the amorphous–crystalline transformation, where the maximum

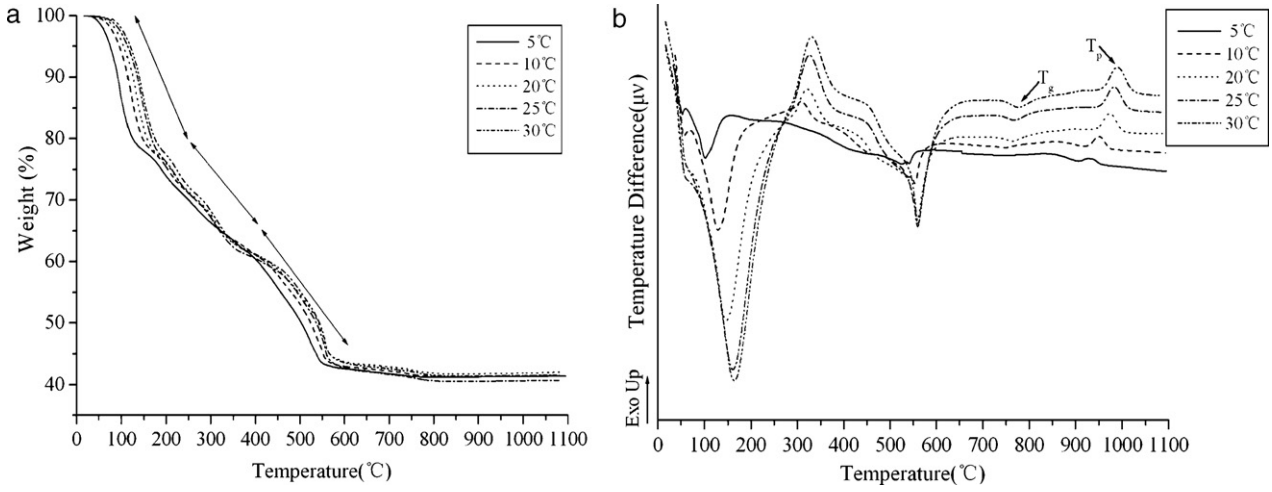

Fig. 1. (a) TG and (b) DTA curves of xerogel at different heating rates.

temperature refers to the crystallization peak temperature (T_p). Most significantly, the exothermic peak becomes broad and shifts to higher temperature with the increase of the heating rate. The values of T_g and T_p recorded at various heating rates are given in Table 2.

Non-isothermal crystallization kinetics of glass can be described using Kissinger equation [19]:

$$\ln\frac{T_p^2}{\beta} = \frac{E_a}{RT_p} + C \quad (1)$$

where β is the heating rate, R is the universal gas constant, C is the constant and E_a is the activation energy of crystal growth. E_a (381 kJ/mol) can be calculated by plots of $\ln(T_p^2/\beta)$ versus $1/T_p$, which are shown in Fig. 2.

The Avrami constant (n) was further evaluated using the Augis–Bennett equation [20]:

$$n = \frac{2.5}{\Delta\tau_{FWHM}} \times \frac{RT_p^2}{E_a} \quad (2)$$

where $\Delta\tau_{FWHM}$ is the width of the exothermic peak at the half maximum intensity. The value of n close to one means that one-dimension growth (surface crystallization) is dominant during crystallization, the value of two indicates two-dimension crystallization, and three implies a significant contribution of three-dimension growth (bulk crystallization) [21–23]. From the results shown in Table 2, it is suggested that the crystallization of glass gradually changes from bulk to surface crystallization with increasing heating rate.

Table 2
The thermal parameters obtained at various heating rates.

β (°C/min)	T_g (°C)	T_p (°C)	E_a (kJ/mol)	n
5	742	934	381	2.92
10	748	951		3.05
20	765	973		2.78
25	770	983		2.51
30	777	990		2.34

3.2. Sample characterization

The evolution of textural properties versus sintering temperature is shown in Fig. 3. The specific surface area (S_{BET}) greatly decreases from 223 to 21 $m^2\ g^{-1}$ between 700 and 900 °C, as shown in Fig. 3(a). The total pore volume (V_t) shows a similar behavior. The sample treated at 900 °C suffers a sharp reduction of the pore volume, reaching a value of 0.056 $cm^3\ g^{-1}$. For samples treated at higher temperatures (1000 and 1200 °C), the values of S_{BET} and V_t are 13 $m^2\ g^{-1}$, 0.038 $cm^3\ g^{-1}$ and 1 $m^2\ g^{-1}$, 0.0048 $cm^3\ g^{-1}$, respectively. Fig. 3(b) shows the plots of pore volumes (V_p) versus diameter (D_p) for the samples treated at various temperatures. A narrow

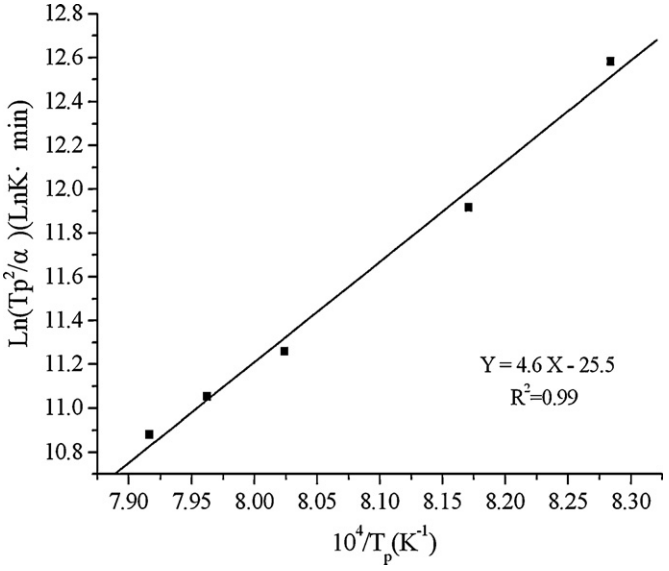

Fig. 2. Plots used for the determination of activation energy (E_a) of crystallization using Kissinger equation.

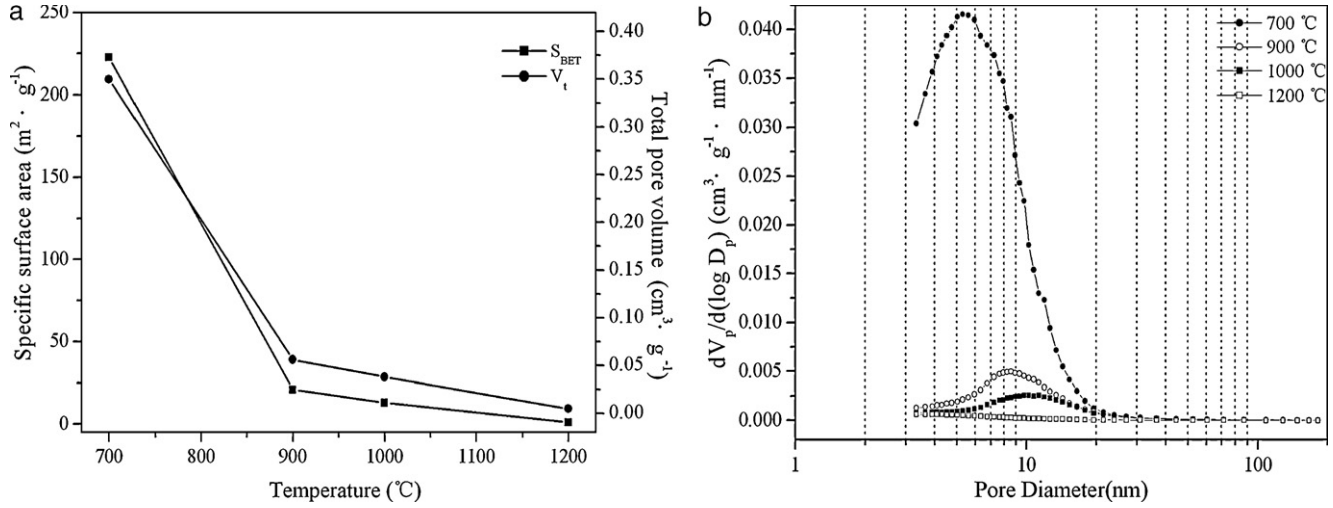

Fig. 3. (a) Specific surface area and total pore volume and (b) pore size distribution of samples obtained at various temperatures.

monomodal distribution centered at 5 and 11 nm is observed for the samples obtained at 700, 900 and 1000 °C, while the distribution for sample treated at 1200 °C is not pronounced.

Fig. 4 shows the XRD patterns of samples sintered at different temperatures. The pattern of sample obtained at 700 °C corresponds to amorphous materials; no crystalline phases were detected. According to the results of TG/DTA, the optimal sintering temperature of glass was determined to be 700 °C, where nitrates have been completely eliminated and the chosen temperature is below the crystallization temperature. For samples sintered at 900 and 1000 °C, pseudowollastonite $Ca_3(Si_3O_9)$ (JCPDS 74-0874) and wollastonite β-$CaSiO_3$ (JCPDS 42-0547) crystal phases were detected, together with some diffraction peaks assigned to akermanite $Ca_2MgSi_2O_7$ (JCPDS 35-0592). At higher temperature (1200 °C), besides the majority phase of wollastonite, crystalline peaks corresponding to akermanite and cristobalite SiO_2 (JCPDS 27-0605) appeared. Compared to the $CaO–P_2O_5–SiO_2$ ternary system sintered at this temperature [24], the incorporation of magnesium induces the formation of new $Ca_2MgSi_2O_7$ crystal phase and promote the crystallization of SiO_2.

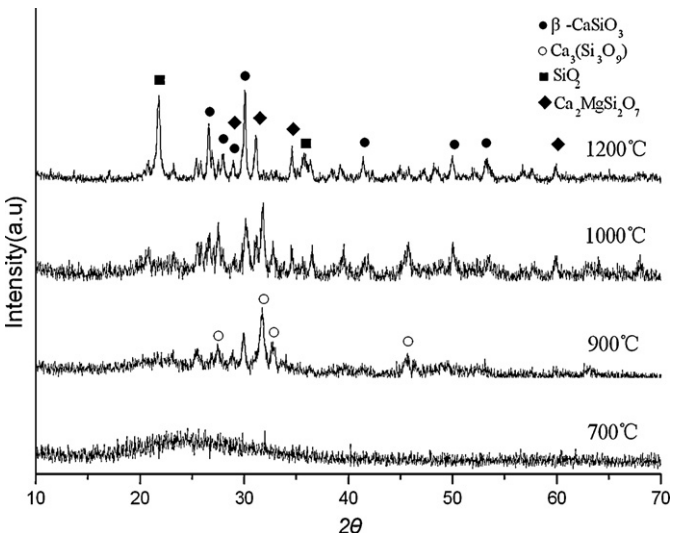

Fig. 4. XRD patterns of samples sintered at various temperatures.

Fig. 5 shows the FTIR spectra of samples obtained at various temperatures. The FTIR spectrum of glass obtained at 700 °C

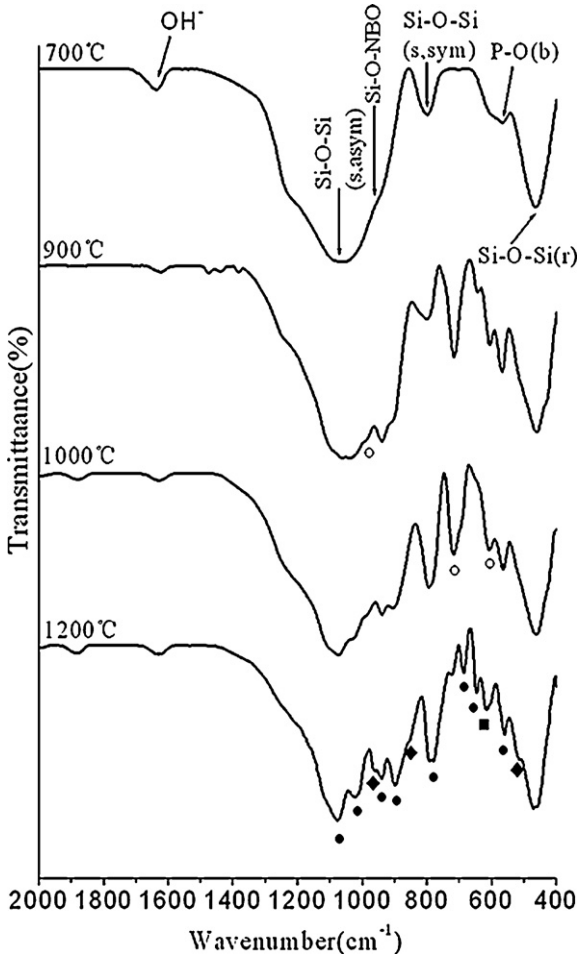

Fig. 5. FTIR spectra of samples obtained at different temperatures. Symbols are related to the vibration modes of pseudowollastonite (○), wollastonite(●), akermanite (◆) and cristobalite(■).

presents characteristic silicate absorption bands [25–28]. The band at 1090 cm^{-1} corresponds to the Si–O–Si(s, asym) asymmetric stretching mode, the one at 800 cm^{-1} is associated to symmetric stretching vibration Si–O–Si(s, sym) and the rocking vibration Si–O–Si(r) is identified at around 460 cm^{-1}. In addition, the shoulder at 950 cm^{-1} related to the non-bridging oxygen bond (NBO) is also detected. Conventionally, magnesium oxide is thought to behave like calcium oxide, as a network modifier, within a silicate glass structure. However, on examination of the Dietzel's ionic field strength I ($I = Z/r^2$, where Z and r is the cation charge and the radius, respectively), Mg^{2+} (4.73 $Å^{-2}$) falls on the boundary between being a network modifier and an intermediate oxide. Watts et al. [29] pointed out that part of magnesium oxide could act as a network intermediate and enter into the silicate network as MgO_4 tetrahedral units. Besides, the peak at 570 cm^{-1} related to the bending vibration P–O (b) and the vibration band around 1630 cm^{-1} due to the deformation mode of H–O–H were also detected [30]. At higher temperatures, in both samples sintered at 900 and 1000 °C, new bands appeared at around 989, 936, 898, 717 and 642 cm^{-1}, which correspond to pseudowollastonite and wollastonite. For the glass-ceramics obtained at 1200 °C, most of the vibration bands were related to the wollastonite besides the band at 620 cm^{-1} corresponding to cristobalite and the vibration bands correlating to akermanite.

The SEM micrographs of glass and glass-ceramics obtained at various temperatures are shown in Fig. 6. For glass obtained at 700 °C, irregular particles with voids among them were observed, as shown in Fig. 6(a). After being sintered at higher temperatures (900–1200 °C), tiny spherical crystallites were observed, and with the increase of the sintering temperatures, grain growth occurred (Fig. 6(b–d)).

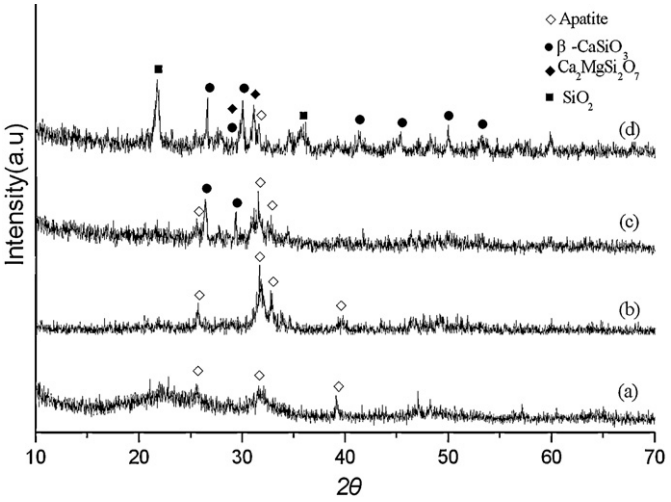

Fig. 7. XRD patterns of samples sintered at (a) 700 °C, (b) 900 °C, (c) 1000 °C and (d) 1200 °C after soaking in SBF for 7 days.

3.3. In vitro tests in SBF

Fig. 7 shows the XRD patterns of glass and glass-ceramics after 7 days soaking in SBF. The XRD pattern of glass sample

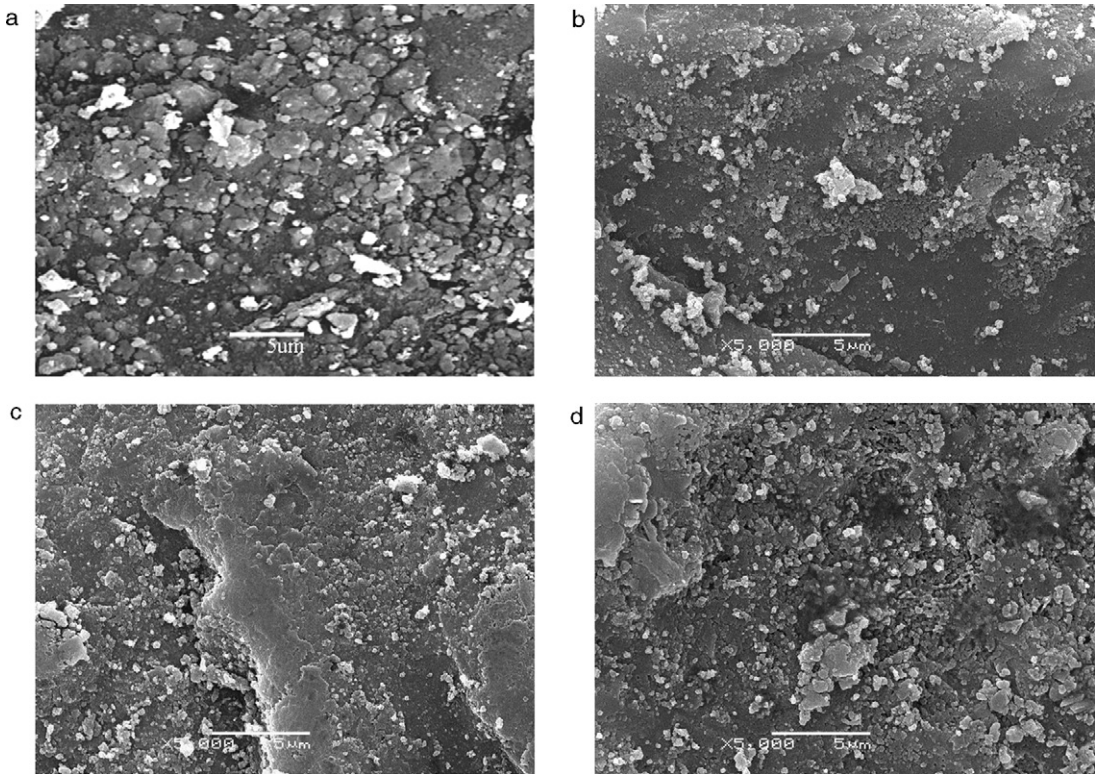

Fig. 6. SEM micrograph of samples sintered at (a) 700 °C, (b) 900 °C, (c) 1000 °C and (d) 1200 °C.

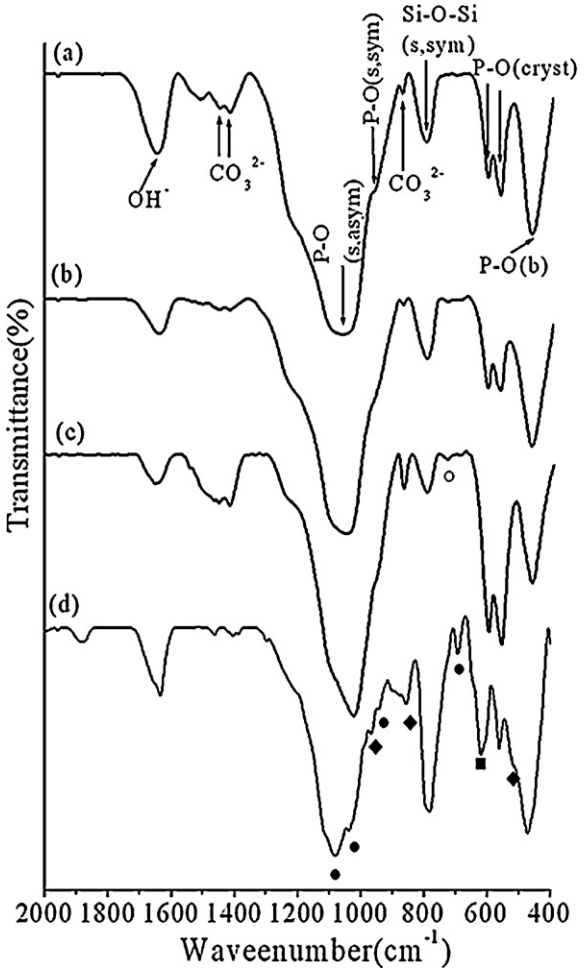

Fig. 8. FTIR spectra of samples sintered at (a) 700 °C, (b) 900 °C, (c) 1000 °C and (d) 1200 °C after 7 days of soaking in SBF. Symbols are related to the vibration modes of pseudowollastonite (○), wollastonite (●), cristobalite (■)) and akermanite (◆).

shows diffraction peaks at 26, 32° and 39° (*2θ*), corresponding to (0 0 2), (2 1 1) and (3 1 0) reflections of the apatite phase (JCPDS 24-0033). For the glass-ceramics obtained at 900 and 1000 °C, the diffraction peaks assigned to apatite were also detected. Moreover, wollastonite was still observed in the glass-ceramics sintered at 1000 °C. In the glass-ceramics obtained at 1200 °C, besides the slight apatite peaks, other diffraction peaks assigned to wollastonite, akermanite and cristobalite phases were also observed. It is worth noting that pseudo-wollastonite and wollastonite diffraction peaks intensity greatly decline after soaking in SBF, which can be attributed to their dissolution [31,32].

The formation of apatite is also confirmed by FTIR. After soaking for 7 days in SBF, glass and glass-ceramics treated at 900 and 1000 °C displayed the doublet bands at 603 and 568 cm^{-1} (Fig. 8(a–c)), which are assigned to crystalline calcium phosphate [33,34]. Moreover, the vibration bands corresponding to the carbonate groups around 1490, 1423 and 874 cm^{-1} were also found, suggesting that CO_3^{2-} ions replaced the PO_4^{3-} site (B site) in the apatite structure [35]. The FTIR spectrum of the glass-ceramics obtained at 1200 °C after 7 days of soaking in SBF (Fig. 8(d)) was similar to that registered before soaking, and the characteristic vibration bands of apatite were slight.

The SEM morphologies of obtained glass and glass-ceramics after soaking in SBF for 7 days are shown in Fig. 9. The samples of glass and glass-ceramics treated at 900 and 1000 °C showed similar behaviors. Formation of apatite can be observed. After soaking for 7 days in SBF, the surface was fully covered by a new layer constituted by numerous spherical particles, however, appreciable morphology differences were also found. Different from above samples, after soaking in SBF, the surface of glass-ceramics prepared at 1200 °C was only partially covered and numerous pores were observed, attributed to the presence of soluble phases in the glass-ceramics.

The in vitro studies in SBF revealed that the incorporation of 10 mol% MgO and crystallization do not suppress the apatite-formation ability of the SiO_2–CaO–MgO–P_2O_5 glass and glass-ceramics. The nucleation and growth mechanism of apatite on the glasses in the system CaO–SiO_2 was proposed by Hench and co-workers [36] It is notified that an interchange between the Ca^{2+} ions of the glass and the H_3O^+ from SBF can give rise to the formation of Si–OH groups on the glass surface that induces the apatite nucleation. According to the above mechanism, it can be expected that the higher the Ca^{2+} release is the faster the apatite is formed. When the sample was treated at a relative lower temperature (700 °C) than that necessary for the crystallization, the amorphous glass sample took a rapid exchange between Ca^{2+} and Mg^{2+} ions locating at the non-bridging oxygen bonds (NBOs) and H_3O^+ from solution. At higher sintering temperatures (900–1200 °C), $Ca_3(Si_3O_9)$, β-$CaSiO_3$ and $Ca_2MgSi_2O_7$ crystal phases were obtained. The crystal phases hindered above ions exchange, and therefore decreased the apatite crystallization and growth. In addition, samples texture (S_{BET} and V_t) greatly decreased with the increase of the sintering temperature, as shown in Fig. 3(a). Apatite deposition in SBF is extensive in rougher regions and sparse in flatter regions. Pereira et al. [37] showed that the rate of apatite formation on a substrate depends on its texture and pointed out that pores may act as nucleation sites where the degree of supersaturation for precipitation of apatite is attained faster.

Although crystallization decreases the samples bioactivity, it does not suppress their apatite-formation ability, even for the glass-ceramics obtained at 1200 °C. For the binary CaO–SiO_2 system, $CaSiO_3$ ceramics are regarded as potential bioactive materials for bone tissue regeneration due to their good bioactivity. However, $CaSiO_3$ ceramics suffer from their high dissolution rate leading to an alkalinization environment, which is deleterious to cell proliferation and limit their application [38]. In this study, $CaSiO_3$–$Ca_2MgSi_2O_7$-based glass-ceramics were successfully prepared. $Ca_2MgSi_2O_7$ phase has been reported to show excellent cytocompatibility and bioactivity, and possesses a significantly lower ionic release rate than $CaSiO_3$, suggesting potential application of $CaSiO_3$–$Ca_2MgSi_2O_7$-based glass-ceramics in skeletal tissue regeneration [39,40].

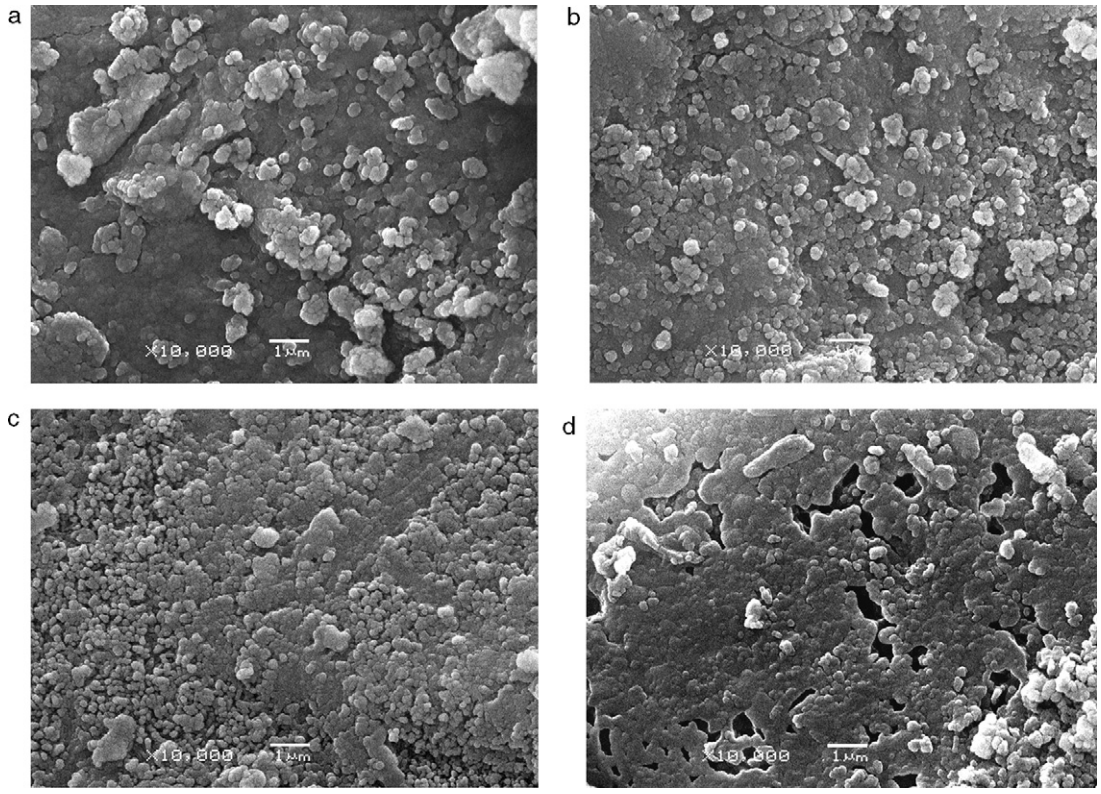

Fig. 9. SEM micrographs of samples sintered at (a) 700 °C, (b) 900 °C, (c) 1000 °C and (d) 1200 °C after soaking in SBF for 7 days.

4. Conclusions

Glass and glass-ceramics in the $CaO–MgO–P_2O_5–SiO_2$ system have been successfully synthesized. Samples texture is greatly influenced by the sintering temperature, and the incorporation of magnesium promotes the crystallization of $Ca_2MgSi_2O_7$ and SiO_2, inducing the formation of $CaSiO_3$–$Ca_2MgSi_2O_7$-based glass-ceramics. In vitro tests indicate that the synthesized glass and glass-ceramics are bioactive, although the crystallization decreases the apatite-formation ability of the glass-ceramics.

Acknowledgements

This work was financially supported by the Key Project of the National Science Foundation of Shandong Province (Grant no: Z2007F02) and Department of Science and Technology of Shandong Province (Grant no: 2006GG3203006), PR China.

References

[1] L.L. Hench, R.J. Splinter, W.C. Allen, T.K. Greenlee, Bonding mechanism at interface of ceramic prosthetic materials, J. Biomed. Mater. Res. 5 (1971) 117–141.
[2] T. Kokubo, Bioactive glass ceramics: properties and applications, Biomaterials 12 (1991) 155–163.
[3] T. Kokubo, S. Ito, Z.T. Huang, T. Hayashi, S. Sakka, T. Kitsugi, T. Yamamuro, Ca, P-rich layer formed on high-strength bioactive glass-ceramic A-W, J. Biomed. Mater. Res. 24 (1990) 331–343.
[4] M. Laczka, K. Cholewa-Kowalaska, A. Laczka-Osyczka, M. Tworzydlo, B. Turyna, Gel-derived materials of a $CaO–P_2O_5–SiO_2$ system modified by boron, sodium, magnesium, aluminum, and fluorine compounds, J. Biomed. Mater. Res. 52 (2000) 601–612.
[5] A.J. Salinas, J. Roman, M. Vallet-Regi, J.M. Oliveira, R.N. Correia, M.H. Fernandes, In vitro bioactivity of glass and glass-ceramics of the $3CaO·P_2O_5–CaO·SiO_2–CaO·MgO·2SiO_2$ system, Biomaterials 21 (2000) 251–257.
[6] A. Martinez, I. Izuierdo-Barba, M. Vallet-Regi, Bioactivity of a $CaO–SiO_2$ binary glasses system, Chem. Mater. 12 (2000) 3080–3088.
[7] W.P. Cao, L.L. Hench, Bioactive materials, Ceram. Int. 22 (1996) 493–507.
[8] I. Gutowska, Z. Machoy, B. Machaliński, The role of bivalent metals in hydroxyapatite structures as revealed by molecular modeling with the HyperChem software, J. Biomed. Mater. Res. Part A 75 (2005) 788–793.
[9] J.M. Oliveira, R.N. Correia, M.H. Fernandez, J. Rocha, Influence of the CaO/MgO ratio on the structure of phase-separated glasses: a solid state ^{29}Si and ^{31}P MAS NMR study, J. Non-Cryst. Solids (2000) 221–229.
[10] C.T. Wu, J. Chang, J.Y. Wang, S.Y. Ni, W.Y. Zhai, Preparation and characteristics of a calcium magnesium silicate (bredigite) bioactive ceramic, Biomaterials 26 (2005) 2925–2931.
[11] E. Landi, G. Logroscino, L. Proietti, A. Tampieri, M. Sandri, S. Sprio, Biomimetic Mg-substituted hydroxyapatite: from synthesis to in vivo behaviour, J. Mater. Sci. Mater. Med. 19 (2008) 239–247.
[12] Y.L. Cai, S. Zhang, X.T. Zeng, Y.S. Wang, M. Qian, W.J. Weng, Improvement of bioactivity with magnesium and fluorine ions incorporated hydroxyapatite coatings via sol–gel deposition on Ti6Al4V alloys, Thin Solid Films 517 (2009) 5351–5437.
[13] M. Vallet-Regí, A.J. Salinas, J. Román, M. Gil, Effect of magnesium content on the in vitro bioactivity of $CaO–MgO–SiO_2–P_2O_5$ sol–gel glasses, J. Mater. Chem. 9 (1999) 515–518.
[14] A. Saboori, M. Rabiee, F. Moztarzadeh, M. Sheikhi, M. Tahriri, M. Karimi, Synthesis, characterization and in vitro bioactivity of sol–gel-derived $SiO_2–CaO–P_2O_5–MgO$ bioglass, Mater. Sci. Eng. C 29 (2009) 335–340.
[15] A. Saboori, M. Sheikhi, F. Moztarzadeh, M. Rabiee, S. Hesaraki, M. Tahriri, N. Nezafati, Sol–gel preparation, characterisation and in vitro

bioactivity of Mg containing bioactive glass, Adv. Appl. Ceram. 108 (2009) 155–161.
[16] T.D. Oulton, The pore size-surface area distribution of a cracking catalyst, J. Phys. Colloid Chem. 52 (1948) 1296–1314.
[17] E.P. Barrett, L.J. Joyner, P.P. Halenda, The determination of pore volume and area distributions in porous substances. I. Computations from nitrogen isotherms, J. Am. Chem. Soc. 73 (1951) 373–380.
[18] T. Kokubo, H. Kushitani, S. Sakka, T. Kitsugi, T. Yamamuro, Solutions able to reproduce in vivo surface-structure changes in bioactive glass-ceramic A-W^3, J. Biomed. Mater. Res. 24 (1990) 721–734.
[19] H.E. Kissinger, Variation of peak temperature with heating rate in differential thermal analysis, J. Res. Natl. Bureau Stand. 57 (1956) 217–221.
[20] J.A. Augis, J.E. Bennett, Calculation of the Avrami parameters for heterogeneous solid-state reactions using a modification of the Kissinger method, J. Therm. Anal. 13 (1978) 283–292.
[21] J. Ma Rincón, M. Romero, J. Marco, V. Caballer, Some aspect of crystallization microstructure on new glass-ceramic glazes, Mater. Res. Bull. 33 (1998) 1159–1164.
[22] A.W.A. Elshennawi, E.M.A. Hamzawy, G.A. Khater, A.A. Omar, Crystallization of some aluminosilicate glasses, Ceram. Int. 27 (2001) 725–730.
[23] M. Romero, J. Ma Rincón, A. Acosta, Effect of iron oxide content on the crystallisation of a diopside glass-ceramic glaze, J. Eur. Ceram. Soc. 22 (2002) 883–890.
[24] J. Ma, C.Z. Chen, D.G. Wang, X.G. Meng, J.Z. Shi, Influence of the sintering temperature on the structure feature and bioactivity of sol–gel derived SiO_2–CaO–P_2O_5 bioglass, Ceram. Int. 36 (2010) 1911–1916.
[25] W. Höland, W. Vogel, K. Naumann, J. Gummel, Interface reactions between machinable bioactive glass-ceramics and bone, J. Biomed. Mater. Res. 19 (1985) 303–312.
[26] S. Radin, P. Ducheyne, B. Rothman, A. Conti1, The effect of in vitro modeling conditions on the surface reactions of bioactive glass, J. Biomed. Mater. Res. Part A 37 (1997) 363–375.
[27] J.L. Arias, F.J. García-Sanz, M.B. Mayor, S. Chiussi, J. Pou, B. León, M. Pérex-Amor, Physicochemical properties of calcium phosphate coatings produced by pulsed laser deposition at different water vapor pressures, Biomaterials 19 (1998) 883–888.
[28] P. Gonzáalez, J. Serra, S. Liste, S. Chiussi, B. León, M. Pérez-Amor, Ageing of pulsed-laser-deposited bioactive glass films, Vacuum 67 (2002) 647–651.
[29] S.J. Watts, R.G. Hill, M.D. O'Donnell, R.V. Law, Influence of magnesia on the structure and properties of bioactive glasses, J. Non-Cryst. Solids 356 (2010) 517–524.
[30] D. Arcos, D.C. Greenspan, M. Vallet-Regí, Influence of the stabilization temperature on textural and structure features and ion release in SiO_2–CaO–P_2O_5 sol–gel glass, Chem. Mater. 14 (2002) 1515–1522.
[31] S. Nita, A. Michel, Cyclic silicate active site and stereochemical match for apatite nucleation on pseudowollastonite bioceramic–bone interfaces, Biomaterials 26 (2005) 5763–5770.
[32] S.Y. Ni, J. Chang, L. Chou, A novel bioactive porous $CaSiO_3$ scaffold for bone tissue engineering, J. Biomed. Mater. Res. Part A 76 (2006) 196–205.
[33] A. Rámila, F. Balas, M. Vallet-Regí, Synthesis routes for bioactive sol–gel glasses: alkoxides versus nitrates, Chem. Mater. 14 (2002) 542–548.
[34] M. Vallet-Regí, A.M. Romero, C.V. Ragel, R.Z. LeGeros, XRD, SEM-EDS, and FTIR studies of in vitro growth of an apatite-like layer on sol–gel glasses, J. Biomed. Mater. Res. Part A 44 (1999) 416–421.
[35] K. Sato, T. Kogure, Y. Kumagai, J. Tanaka, Crystal orientation of hydroxyapatite induced by ordered carboxyl groups, J. Colloid Interface Sci. 240 (2001) 133–138.
[36] O. Peitl, E.D. Zanotto, L.L. Hench, Highly bioactive P_2O_5–Na_2O–CaO–SiO_2 glass-ceramics, J. Non-Cryst. Solids 292 (2001) 115–126.
[37] M.M. Pereira, A.E. Clark, L.L. Hench, Effect of texture on the rate of hydroxyapatite formation on gel-silica surface, J. Am. Ceram. Soc. 78 (1995) 463–468.
[38] Y. Iimori, Y. Kameshima, K. Okada, S. Hayashi, Comparative study of apatite formation on $CaSiO_3$ ceramics in simulated body fluids with different carbonate concentrations, J. Mater. Sci. Mater. Med. 16 (2005) 73–79.
[39] C.T. Wu, J. Chang, Degradation, bioactivity, and cytocompatibility of diopside, akermanite, and bredigite ceramics, J. Biomed. Mater. Res. Part B 83 (2007) 153–160.
[40] C.T. Wu, J. Chang, A novel akermanite bioceramic: preparation and characteristics, J. Biomater. Appl. 21 (2006) 119–129.